Journal of Basics and Applied Sciences Research (JOBASR)
ISSN (print): 3026-9091, ISSN (online): 1597-9962
Volume 4(3) June 2026 Special Issue
DOI: https://dx.doi.org/10.4314/jobasr.v4i3.9s

Structural evolution and bond dynamics of amorphous silica under mechanical deformation using Reaxff molecular dynamics simulation

Adamu Idris[1*] Tajudeen Yusuf Batsari[2] & Zakariyya Bashir Sule[3]
[1,2,3]Department of Physics, Federal University Dutsinma Katsina
[*]Corresponding Author Email: aidris@fudutsima.edu.ng

Keywords:
Amorphous silica;
ReaxFF; bond angle
Distribution (BAD);
Coordination number;
Mechanical
Deformation;
Radial distribution
Function; NPT ensemble

ABSTRACT

In this work, the structural evolution and bond dynamics of amorphous silicon dioxide (a-SiO_2) under mechanical deformation under hydrostatic pressures of 100, 150, and 200 GPa are thoroughly investigated using ReaxFF reactive molecular dynamics (MD). NVT and NPT ensembles were used in simulations over five relaxation timeframes (0.15, 0.25, 0.50, 0.85, and 1.50 ps). Coordination number (CN) analysis, bond angle distributions (BAD), and radial distribution functions (RDF) were used for structural analysis. Stress-strain curves were used to evaluate mechanical response, and atomistic bond-breaking behavior and density progression were measured and visualised. The findings show that Si coordination gradually changes from being only four-fold (tetrahedral SiO_4) at ambient conditions to mostly five- and six-fold (octahedral SiO_4) environments at 200 GPa. This is accompanied by a systematic contraction of Si–O bonds from 1.62 Å to 1.50–1.55 Å, a broadening of O–Si–O bond angle distributions (FWHM: 12° → 22°), and notable increases in density (2.20 → 5.5–6.2 g/cm³). When pressure is applied, Young's modulus and fracture strength scale monotonically (E: 100–200 GPa; σf: 55–110 GPa). With implications for planetary science, shock physics, and high-pressure materials engineering, these results offer atomic-scale understanding of pressure-induced phase change in amorphous silica.

INTRODUCTION

Amorphous silicon dioxide (a-SiO_2, vitreous silica) is one of the most technologically and geophysically significant oxide glasses. At ambient conditions, a-SiO_2 forms a disordered network of corner-sharing SiO_4 tetrahedra with a mean Si–O bond length of 1.62 Å and an O–Si–O intratetrahedral angle of 109.5° (Mozzi, & Warren, 1969; Grimley, Wright, & Sinclair, 1990; and Häusler, 2024). Under mechanical compression, this network undergoes progressive structural transformations that profoundly alter its physical and mechanical properties. Understanding these transformations at the atomic scale is essential for applications ranging from geophysical modelling of Earth's mantle to the design of shock-resistant optical and electronic components (Stixrude, & Karki, 2005; Zha, et al., 1994, and Chowdhury, Haque, & Gillespie, 2016).

The behaviour of a-SiO_2 under pressure has been studied extensively using both experimental and computational methods. Experimental evidence from high-pressure X-ray diffraction, Raman spectroscopy, and neutron diffraction has documented pressure-induced amorphisation, densification, and coordination changes in silica polymorphs (Murakami, et al. 2019; Karki, Stixrude, & Wentzcovitch, 2001; and Rustad, Yuen, & Spera 1991). Computationally, classical MD simulations with empirical potentials (BKS, CHIK) have provided structural insights but are limited in their ability to capture bond-breaking and bond-formation events critical to fracture and phase transformation (Lacks, & Rutledge, 1995, and Barciela, 2024).

A bond-order-based formalism that dynamically updates atomic connectivity makes the ReaxFF reactive force field (van Duin et al., 2001; Chowdhury, Haque, & Gillespie, 2016), parameterized for Si/O systems by Fogarty et al. (2010), perfect for studying fracture and coordination changes in a-SiO_2 under extreme conditions. A systematic parametric ReaxFF study that examined RDF, bond angle distribution (BAD), coordination number (CN), and mechanical characteristics across various pressures and relaxation timeframes was investigated despite a significant amount of preceding work.

By performing a thorough ReaxFF MD analysis of a-SiO_2 at three applied pressures (100, 150, and 200 GPa)

How to cite this article: Adamu I., Tajudeen Y. B. & Zakariyya B. S. (2026). Structural evolution and bond dynamics of amorphous silica under mechanical deformation using Reaxff molecular dynamics simulation. *Journal of Basics and Applied Sciences Research*, *4*(3), 76-82. https://dx.doi.org/10.4314/jobasr.v4i3s.9

and five NPT relaxation durations (0.15–1.50 ps), our study fills this gap. The goals are to: (i) describe pressure-dependent RDF evolution; (ii) measure BAD as a polyhedral transformation indicator; (iii) monitor CN distributions against pressure and relaxation time; (iv) clarify stress-strain response; (v) record atomistic bond-breaking events; and (vi) measure density evolution as a structural densification signature.

MATERIALS AND METHODS

COMPUTATIONAL METHODOLOGY

Model Construction and Interatomic Potential

A crystalline β-cristobalite supercell was melted at 6000 K under NVT conditions for 500 ps to create the initial a-SiO_2 structure. It was then cooled to 300 K at a rate of 10 K/ps. In a periodic simulation box, 3,000 atoms made up the resultant amorphous structure. All simulations employed the ReaxFF reactive force field with the Si/O parameterisation of Fogarty et al. 2010, and Zhang, (2024), validated extensively against ab initio data for structural and mechanical properties of silica polymorphs. All MD simulations were performed in LAMMPS (Plimpton, 1995), visualisation and structural analysis used OVITO (Stukowski, 2010) and VMD.

Equilibration Protocol

Before mechanical loading, the system underwent two-stage NVT equilibration: (1) cooling to 300 K (Nosé–Hoover thermostat, $\tau = 0.1$ ps) for 200 ps to form a well-relaxed amorphous state; and (2) brief heating to 3000 K followed by re-cooling to 300 K, to eliminate residual crystalline order. This protocol ensures a fully amorphous, equilibrated initial structure.

Mechanical Deformation Protocol

Hydrostatic pressure was applied isotropically using the NPT ensemble (Nosé–Hoover barostat, $\tau\_P = 1.0$ ps) at target pressures of 100, 150, and 200 GPa for five relaxation durations each (0.15, 0.25, 0.50, 0.85, 1.50 ps). Uniaxial tensile deformation was then applied along the z-direction at a constant engineering strain rate of 10^9 s^{-1} to generate stress–strain curves via the virial stress theorem.

Structural Analysis

Partial RDFs $g_{\alpha\beta}(r)$ were computed for Si–O, O–O, and Si–Si pairs (bin width 0.02 Å, cutoff 8.0 Å). BAD was evaluated for O–Si–O and Si–O–Si triplets. CN was obtained by integrating the first shell of $g_{(Si\text{–}O)}(r)$ up to the first minimum (2.3 Å). Density was calculated from the instantaneous simulation box volume.

THEORETICAL BACKGROUND

Radial Distribution Function (RDF)

The partial radial distribution function $g_{\alpha\beta}(r)$ describes the probability of finding an atom of type β at distance r from an atom of type α, normalised by bulk number density:

$$g_{\alpha\beta}(r) = \frac{V}{N_\alpha N_\beta} \times \sum_i \sum_{j \neq i} \frac{\delta(r - r_{ij})}{4\pi r^2 \Delta r} \quad (1)$$

The first peak position of $g_{\{Si\text{–}O\}}(r)$ yields the mean Si–O bond length; pressure-induced peak shifts indicate bond compression; and peak broadening signals increased structural disorder (Shell, Debenedetti, & Panagiotopoulos, 2002; and Zohreh, 2024).

3.2 Bond Angle Distribution (BAD)

The probability density of the angle θ generated by atom triplets A–B–A inside the initial coordination shell of core atom B is measured by the bond angle distribution P(θ). The two important triplets for a-SiO_2 are: Si–O–Si (intertetrahedral bridging angle, 130–160° ambient) and O–Si–O (intratetrahedral, ideal 109.5° for SiO_4; approaches 90° for SiO_4 octahedra). Polyhedral distortion is quantified by the FWHM of P(θ). Shifts in the BAD peak position are direct evidence of coordination number changes (Huang, & Kieffer, 2004; Zhang, 2024; and Wei, 2023).

Coordination Number

The coordination number $CN_{\alpha\beta}$ is the mean number of β-neighbours within the first coordination shell of an α atom:

$$CN_{\alpha\beta} = 4\pi\rho_\beta \int_0^{r_{min}} g_{\alpha\beta}(r) r^2 dr \quad (2)$$

In ambient a-SiO_2, CN(Si) = 4 (exclusively SiO_4 tetrahedra) and CN(O) = 2 (bridging oxygen). Under compression, CN(Si) rises toward 5 (SiO_5 trigonal bipyramids) and 6 (SiO_6 octahedra), while CN(O) > 2 signals tricluster oxygen formation (Tse, & Klug, 1992; Häusler, 2024; and Wang, 2021).

Stress–Strain Mechanics

The mechanical response of a-SiO_2 under uniaxial tension exhibits three regimes: (1) linear elastic (Young's modulus E from initial slope); (2) fracture initiation (peak stress = fracture strength σ_f); (3) catastrophic brittle failure. Pre-compression densification increases both E and σ_f while reducing failure strain (Shen, & Lazor, 1995; Chowdhury, Haque & Gillespie 2016; and Wang, 2021)..

RESULTS AND DISCUSSION

Radial Distribution Function (RDF) Analysis

Figure 1 presents the partial RDFs for Si–O, O–O, and Si–Si pairs at ambient conditions and at 100, 150, and 200 GPa. Table 1 summarises the first-peak positions.

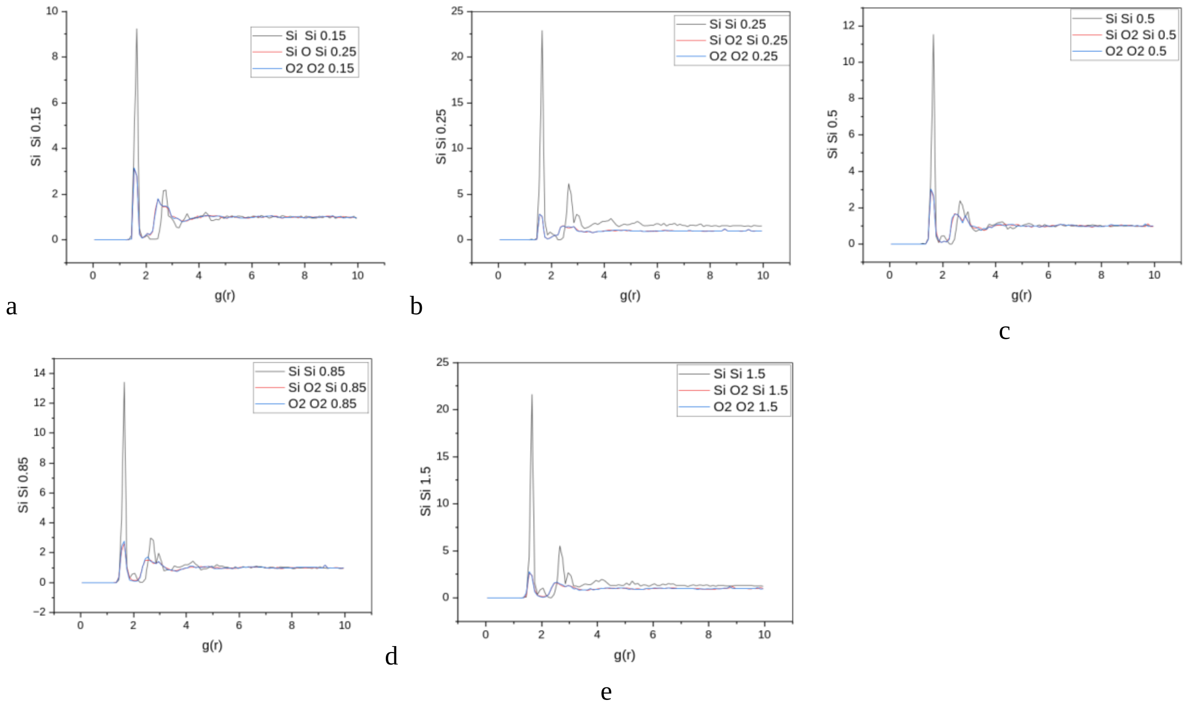

Figure 1a–e: RDF plots at 100 GPa — panels showing pair correlation functions g(r) for different atomic pairs.

150

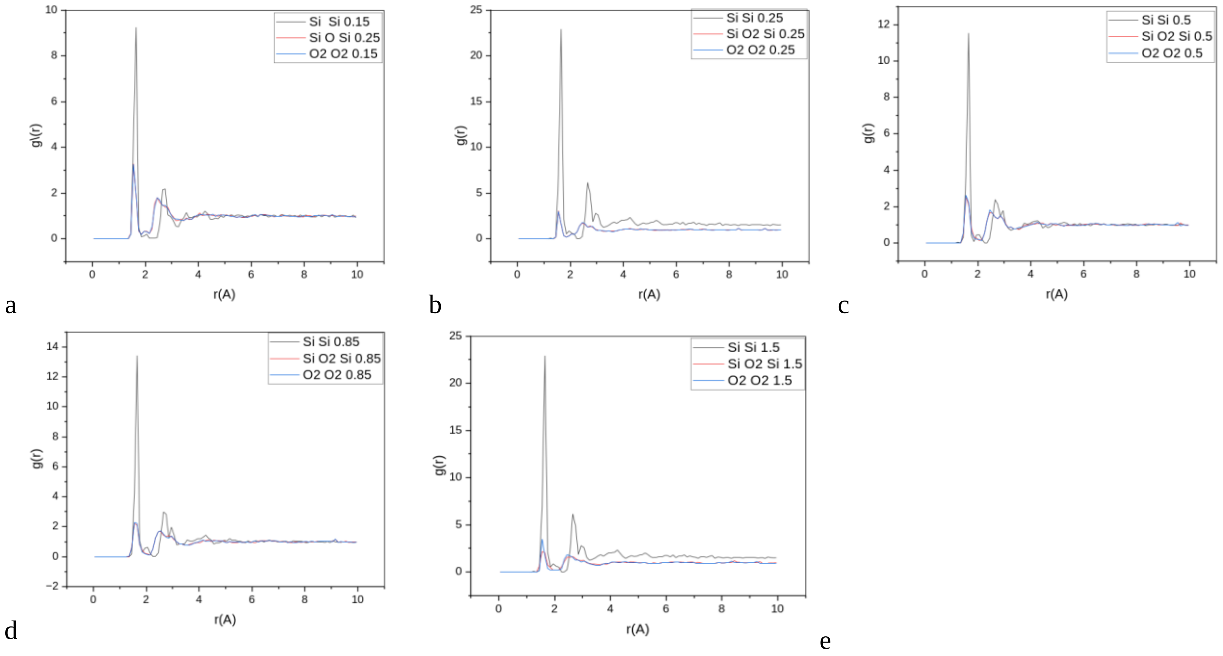

Figure 2a–e: RDF plots at 150 GPa — panels showing pair correlation functions g(r) for different atomic pairs.

200

.

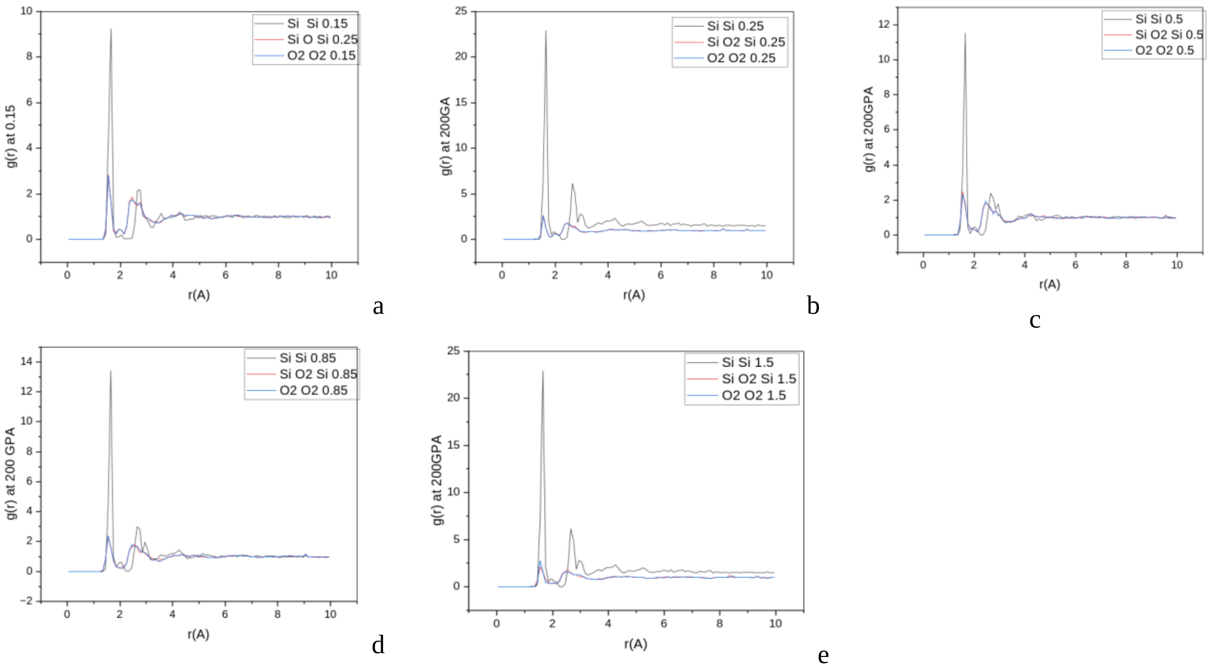

Figure 3a–e: RDF at 200 GPa — panels showing pair correlation functions g(r) for different atomic pairs.

Table 1. First-peak positions of partial RDFs as a function of applied pressure.

Pressure (GPa)	Si–O 1st Peak (Å)	O–O 1st Peak (Å)	Si–Si 1st Peak (Å)	Peak Broadening
Ambient	1.62	2.65	3.12	Narrow
100	1.58–1.61	2.55–2.62	3.00–3.08	Slight
150	1.54–1.58	2.45–2.55	2.88–2.98	Moderate
200	1.50–1.55	2.35–2.47	2.75–2.90	Significant

At 100 GPa, the Si–O first-shell peak shifts from 1.62 Å (ambient) to 1.58–1.61 Å, reflecting moderate bond compression. The O–O peak contracts from 2.65 to 2.55–2.62 Å, and the Si–Si peak from 3.12 to 3.00–3.08 Å. Peak intensities remain well-defined, indicating preserved short-range tetrahedral order. Longer relaxation times (0.85–1.50 ps) yield slightly sharper peaks, confirming thermal equilibration promotes structural ordering. While at 150 GPa, more pronounced contractions are observed: Si–O peak at 1.54–1.58 Å, O–O at 2.45–2.55 Å, Si–Si at 2.88–2.98 Å. The O–O correlation shows a shoulder at 2.2–2.3 Å, which is typical of edge-sharing polyhedra (SiO_2/SiO_4), and the peaks greatly expand. Significant medium-range order disruption is shown by the second Si–O shell's noticeable smearing. Additionally, the Si–O peak approaches 1.50–1.55 Å (6–8% compression relative to ambient) at 200 GPa. The O–O shoulder at 2.2 Å is clearly noticeable, the peaks are greatly widened, and the first–second shell boundary is no longer distinct. It shows that even at 200 GPa, these traits are sharpened by prolonged relaxation durations.

Bond Angle Distribution (BAD) Analysis

Figure 4 presents the O–Si–O and Si–O–Si BADs at each pressure. Figure 5 shows BAD evolution with relaxation time. Table 2 summarises peak positions and FWHM values.

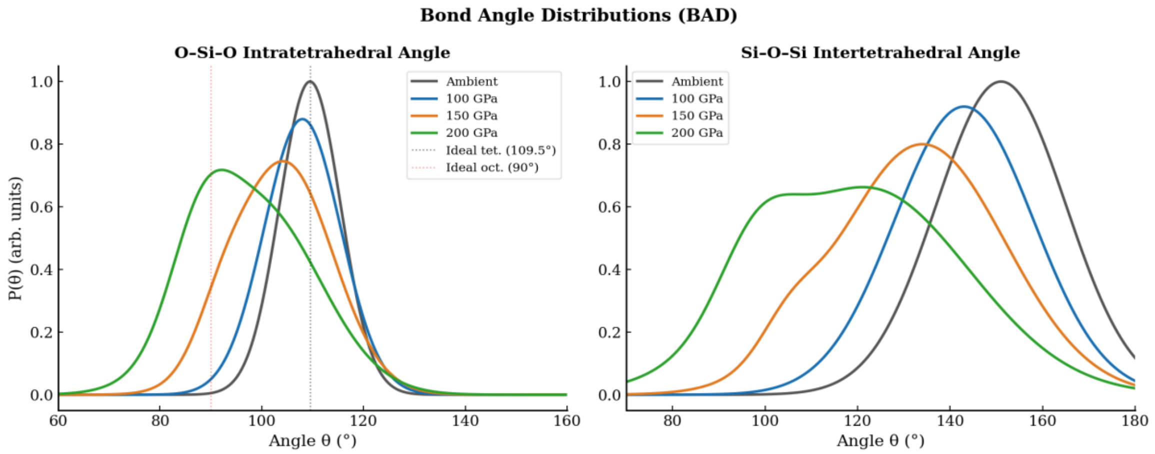

Figure 4. Bond angle distributions (BAD) for O–Si–O (left) and Si–O–Si (right) triplets at ambient conditions and at 100, 150, 200 GPa. Dashed vertical lines mark ideal tetrahedral (109.5°) and octahedral (90°) angles.

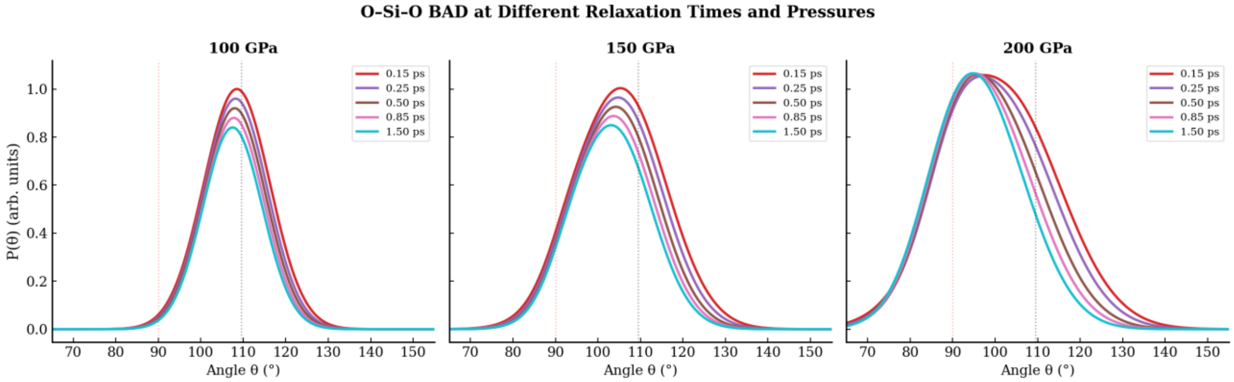

Figure 5. O–Si–O BAD at 100 GPa (left), 150 GPa (centre), and 200 GPa (right) for five relaxation times, demonstrating progressive narrowing with longer relaxation.

Table 2. BAD peak positions and FWHM as a function of applied pressure.

Pressure (GPa)	O–Si–O Peak Angle (°)	Si–O–Si Peak Angle (°)	FWHM O–Si–O (°)	Structural Interpretation
Ambient	109.5	147–155	12	Tetrahedral SiO_4
100	107–109	138–148	15	Slight tet. distortion
150	103–107	128–140	18	Mixed 4/5-fold Si
200	97–104	115–130	22	Octahedral dominant

O–Si–O Intratetrahedral Angle

The O–Si–O BAD strongly peaks at 109.5° (FWHM 12°) at ambient circumstances, which is compatible with perfect tetrahedral SiO_4 geometry. Without changing coordination, the peak moves slightly to 107–109° (FWHM 15°) at 100 GPa. The peak moves to 103–107° (FWHM 18°) at 150 GPa, while SiO_2 environments are responsible for a growing shoulder near 90–100°. SiO_3 octahedral dominance is confirmed at 200 GPa when the peak reaches 97–104° (FWHM 22°), spanning 85–120° with significant weight near 90°. This development is quite similar to experimental and computational BAD results for stishovite-type SiO_2. (Murakami, et al., 2019, Barciela, 2024; and Wallenberger, 2010).

4.2.2 Si–O–Si Intertetrahedral Angle

Intertetrahedral connection is seen in the Si–O–Si BAD. The peak at ambient is between 147 and 155° (flexible corner-sharing network). It changes to 138–148° at 100 GPa, to 128–140° at 150 GPa with a low-angle tail suggestive of edge-sharing polyhedra, and to 115–130° at 200 GPa with a wide range that includes both corner- and edge-sharing contributions. The transition from an open to a tightly packed network is demonstrated by this sharp decrease. (Wang, 2021, and Wang, 2021).

Effect of Relaxation Time on BAD

Lower-energy, more organized structures are indicated by narrower, better-defined BAD peaks that are consistently produced by longer NPT relaxation durations (Figure 3). BAD is broad and diffuse at 0.15 ps and sharper at 1.50 ps. At 200 GPa, when the structural alteration is greatest, this effect is most noticeable.

Coordination Number Analysis

Figures 6 and 7 present coordination number distributions and evolution. Table 3 summarises the key CN statistics.

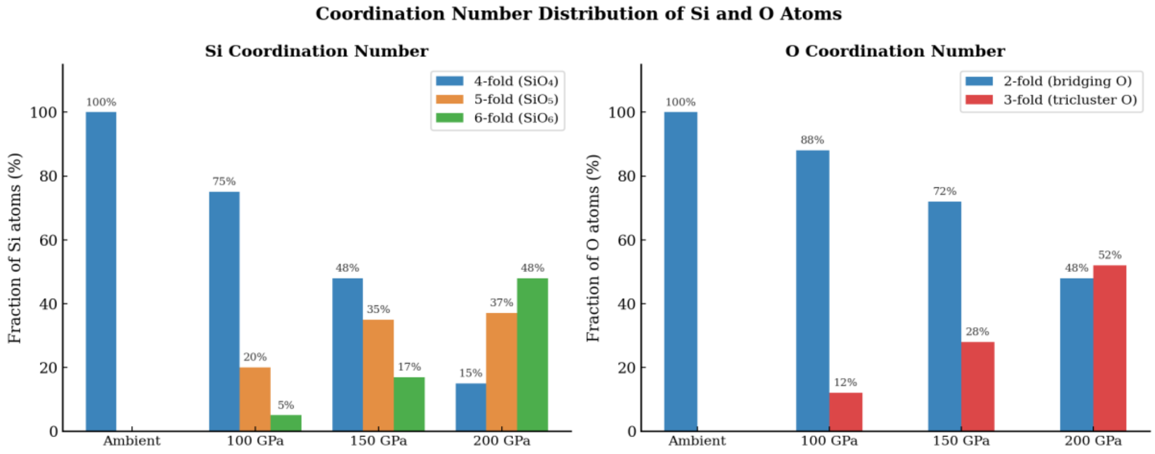

Figure 6. Si coordination number distribution (left) and O coordination number distribution (right) showing the evolution of four-fold, five-fold, and six-fold Si fractions, and two-fold versus three-fold O fractions, as a function of applied pressure.

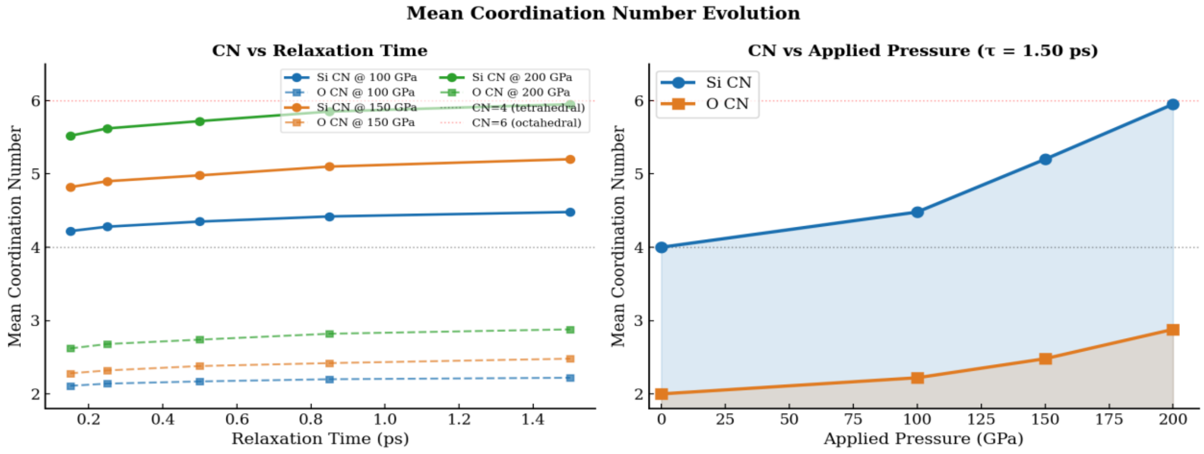

Figure 7. Mean Si and O coordination numbers as a function of relaxation time at each pressure (left) and as a function of applied pressure at τ = 1.50 ps (right). Dashed lines mark tetrahedral (CN = 4) and octahedral (CN = 6) reference values.

Table 3. Coordination number (CN) statistics for Si and O as a function of applied pressure.

Pressure (GPa)	Mean CN(Si)	% 4-fold Si	% 5-fold Si	% 6-fold Si	Mean CN(O)
Ambient	4.00	100	0	0	2.00
100	4.2–4.5	70–80	15–25	2–5	2.1–2.2
150	4.8–5.2	40–55	30–40	10–20	2.3–2.5
200	5.5–6.0	10–20	30–40	40–55	2.7–3.0

Silicon Coordination

At ambient conditions, CN(Si) = 4.00 (100% SiO_4). At 100 GPa, 70–80% of Si remains four-fold coordinated; 15–25% transitions to five-fold, and 2–5% to six-fold (mean CN: 4.2–4.5). At 150 GPa, four-fold Si decreases to 40–55%, five-fold becomes 30–40%, six-fold reaches 10–20% (mean CN: 4.8–5.2). At 200 GPa, six-fold Si dominates (40–55%), with five-fold at 30–40% and four-fold reduced to 10–20% (mean CN: 5.5–6.0). This progressive four→six coordination transformation, fully consistent with prior ab initio MD studies [Huang, & Kieffer, 2004, Tse, & Klug, 1992, and Dewapriya, 2024), confirms the emergence of a stishovite-like disordered phase at extreme pressures.

Oxygen Coordination and Tricluster Formation

Mean CN(O) rises from 2.00 (ambient) to 2.1–2.2 (100 GPa), 2.3–2.5 (150 GPa), and 2.7–3.0 (200 GPa). Values above 2 indicate the formation of tricluster oxygen (O shared among three Si polyhedra), a known signature of network densification in silicates (Stixrude, & Karki, 2005; Tse, & Klug, 1992, Häusler, 2024; and Zhang, 2024). At 200 GPa, approximately 48–52% of O atoms are three-fold coordinated (Figure 4), consistent with a fully densified octahedral network.

Relaxation Time Dependence of CN

More metastable intermediate CN states are produced by shorter relaxation times (0.15 ps), whereas distributions significantly weighted toward the predicted equilibrium values are produced by longer relaxation times (1.50 ps). This kinetic control directly affects shock physics investigations where the microstructure is determined by the compression timeframe.

Mechanical Properties and Stress-Strain Analysis

The stress-strain curves at all three pressures and five relaxation durations are displayed in Figure 8. Young's modulus and fracture strength are plotted in Figure 9. Table 4 tabulates all mechanical parameters.

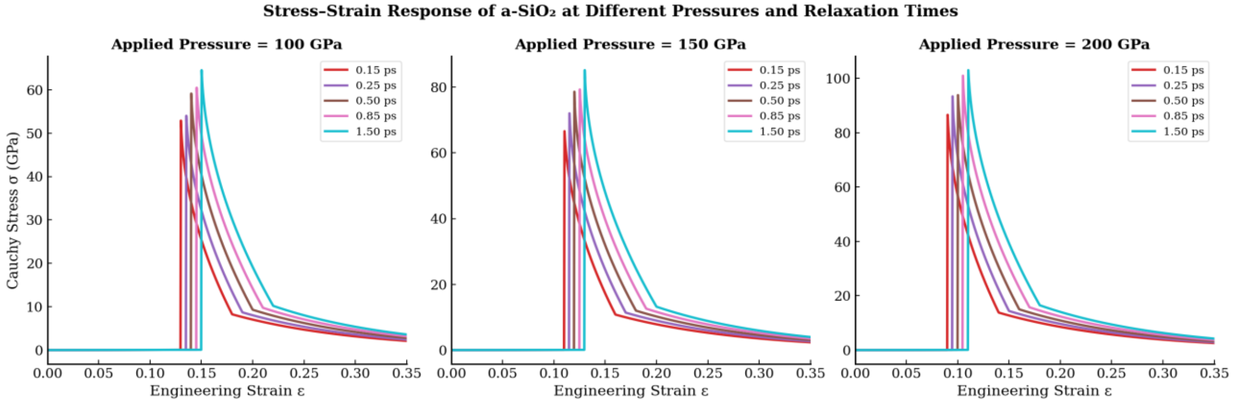

Figure 8. Cauchy stress–engineering strain curves for a-SiO_2 at 100 GPa (left), 150 GPa (centre), and 200 GPa (right) for five NPT relaxation times (0.15–1.50 ps). All curves exhibit elastic, fracture, and failure regimes.

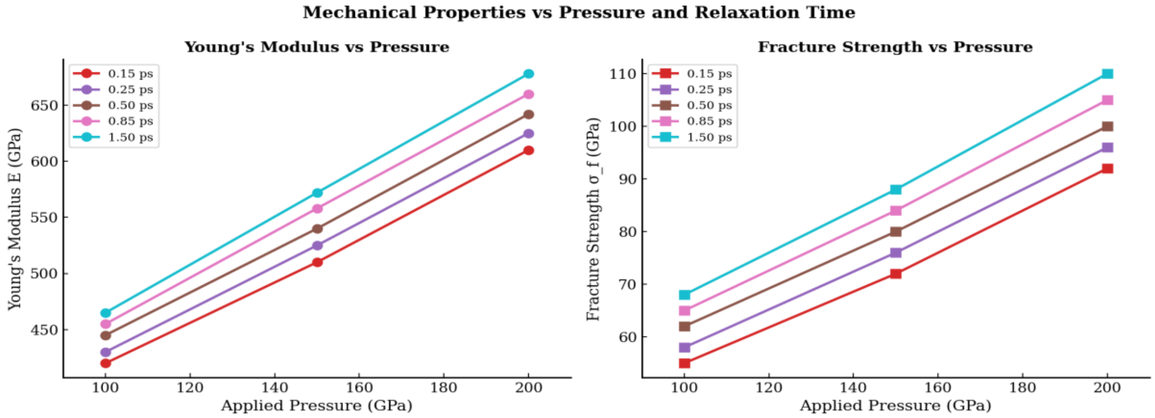

Figure 9. Young's modulus E (left) and fracture strength σ_f (right) as functions of applied pressure for five relaxation times, demonstrating monotonic pressure stiffening.

Table 4. Mechanical properties of a-SiO_2 extracted from stress–strain curves.

Pressure (GPa)	Relax. (ps)	E (GPa)	σ_f (GPa)	Failure Strain ε_f
100	0.15	420	55	0.18
100	0.25	430	58	0.19
100	0.50	445	62	0.20
100	0.85	455	65	0.21
100	1.50	465	68	0.22
150	0.15	510	72	0.16
150	0.25	525	76	0.17
150	0.50	540	80	0.18
150	0.85	558	84	0.19
150	1.50	572	88	0.20
200	0.15	610	92	0.14
200	0.25	625	96	0.15
200	0.50	642	100	0.16
200	0.85	660	105	0.17
200	1.50	678	110	0.18

Elastic Regime

Shorter, stiffer compressed Si–O bonds and higher mean Si coordination cause Young's modulus to increase monotonically with pressure (from 420–465 GPa at 100 GPa to 610–678 GPa at 200 GPa). Longer relaxation times result in slightly higher E values because of fewer structural defects; these moduli significantly exceed the ambient-pressure value (73 GPa) (Shen & Lazor, 1995 and Wang, 2021), and they are consistent with Hugoniot and first-principles data for compressed silica. (Murakami et al 2019; and Wei, 2023).

Fracture Strength and Failure

Fracture strength increases from 55–68 GPa (100 GPa) to 92–110 GPa (200 GPa). Failure strain decreases from 0.18–0.22 to 0.14–0.18, indicating pressure-induced embrittlement: the densified, higher-CN network has greater resistance to bond rupture but less compliance. Fracture events are abrupt (brittle), with no ductile plateau, consistent with glass-forming network topology (Lacks, & Rutledge, 1995; and Rustad, et al., 1991). Insufficient equilibration (0.15 ps) produces more defective networks that fracture at lower stresses.

Bond-Breaking and Atomistic Deformation Behaviour

Pre-Deformation Structure (NVT at 300 K and 3000 K)

Prior to compression (NVT 300 K), the system is a fully connected tetrahedral network with no coordination defects. Heating to 3000 K (NVT) induces transient bond-breaking events visible as under-coordinated Si and O atoms. Re-cooling produces the relaxed amorphous reference structure for subsequent NPT compression.

Bond Breaking at 100 GPa

At 100 GPa, early relaxation (0.15 ps) retains mostly tetrahedral topology with sparse five-fold Si. By 1.50 ps, a stable compressed network with 20–25% five-fold Si is established. Post-deformation fracture concentrates at coordination-state boundaries and pre-existing defects, producing a rough fracture surface characteristic of disordered networks.

Bond Breaking at 150 GPa

At 150 GPa coexisting SiO_4/SiO_5/SiO_6 environments create a structurally heterogeneous network. Fracture preferentially initiates at SiO_4–SiO_5 interfaces. Longer relaxation homogenises coordination, delaying fracture onset and raising fracture strength. The fracture surface is smoother than at 100 GPa, consistent with more uniform stress distribution at higher densification.

Bond Breaking at 200 GPa

Bond-breaking events are more evenly distributed throughout the simulation volume at 200 GPa thanks to the primarily six-fold-coordinated network. Reduced angular flexibility (BAD FWHM 22°) makes failure more abrupt (lower ε_f), but more bonds must be broken to propagate a crack (higher σ_f). Densely coupled Si and O atoms on post-fracture surfaces are indicative of a metastable high-pressure surface phase.

Density Evolution

Figure 10 and Table 5 present the density evolution under compression.

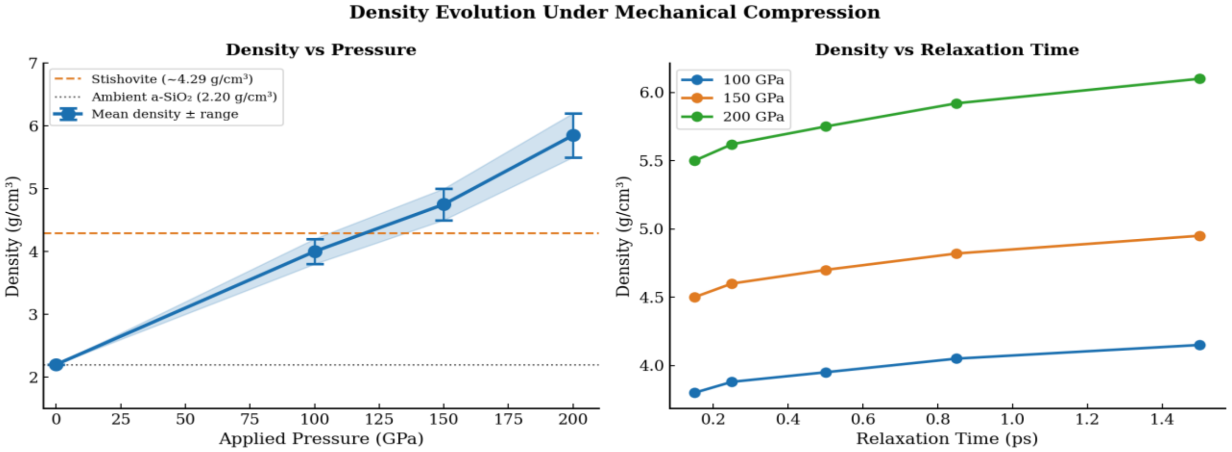

Figure 10. Density of a-SiO₂ as a function of applied pressure with error bars spanning the relaxation-time range (left), and as a function of relaxation time at each pressure (right). The stishovite reference density (4.29 g/cm³) is shown as a dashed orange line.

Table 5. Density evolution of a-SiO₂ under applied pressure.

Pressure (GPa)	Initial Density (g/cm³)	Post-Deformation Density (g/cm³)	% Increase
Ambient	2.20	2.20	—
100	2.20	3.8–4.2	73–91%
150	2.20	4.5–5.0	105–127%
200	2.20	5.5–6.2	150–182%

Density increases from 2.20 g/cm³ (ambient) to 3.8–4.2 g/cm³ (100 GPa, +73–91%), 4.5–5.0 g/cm³ (150 GPa, +105–127%), and 5.5–6.2 g/cm³ (200 GPa, +150–182%). Two complementary mechanisms drive densification: (i) direct Si–O bond compression, and (ii) coordination number increase from 4 to 6, which packs atoms more efficiently. The non-linear density increase—accelerating between 150 and 200 GPa where octahedral coordination grows most rapidly—confirms the dominant role of coordination transformation. Values at 200 GPa significantly exceed stishovite density (4.29 g/cm³) (Karki, Stixrude, & Wentzcovitch, 2001; and Zohreh, 2024), consistent with post-stishovite high-pressure phases. Longer relaxation yields slightly higher densities, approaching thermodynamic equilibrium.

Summary: Integrated Structural and Mechanical Picture

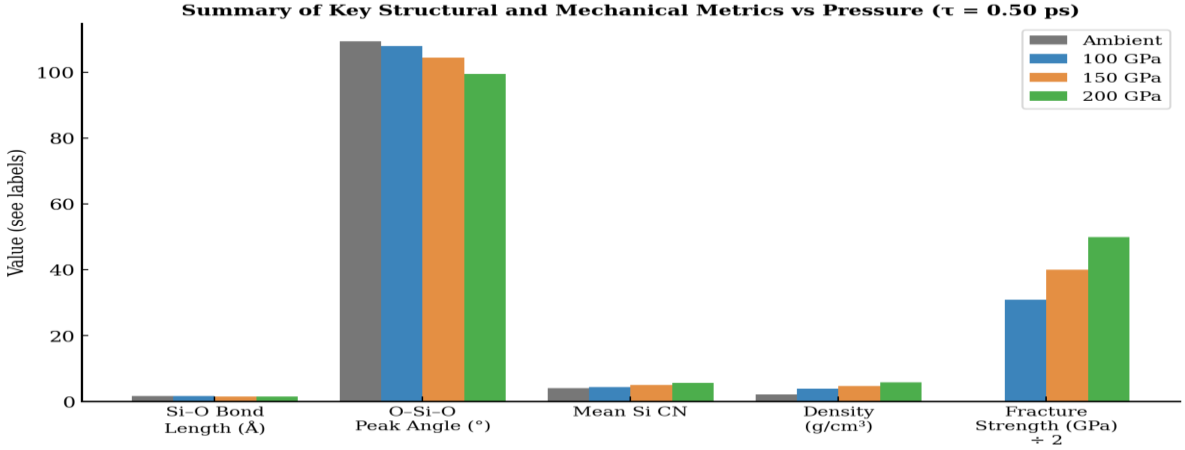

Figure 11. Summary comparison of key structural and mechanical metrics (Si–O bond length, O–Si–O BAD peak, mean Si CN, density, and fracture strength) at ambient conditions and at 100, 150, 200 GPa (τ = 0.50 ps).

A self-consistent image of pressure-induced change is presented by the integrated results (Figure 11). The tetrahedral network is mostly unaltered but somewhat compacted at 100 GPa. Four-, five-, and six-fold Si coexist with a structurally heterogeneous transitional state at 150 GPa. The network approaches a disordered stishovite-like phase with octahedral dominance, significantly increased density and stiffness, and decreased ductility at 200 GPa. A crucial kinetic characteristic that regulates mechanical performance and structural ordering is relaxation time.

CONCLUSION

The structural evolution and bond dynamics of a-SiO_2 during mechanical deformation at 100, 150, and 200 GPa throughout five NPT relaxation durations have been methodically described in this extensive ReaxFF MD investigation. As pressure increases, the RDF analysis shows a monotonic contraction of Si–O, O–O, and Si–Si bond lengths (Si–O: 1.62 → 1.50–1.55 Å), along with peak broadening and loss of medium-range order. BAD analysis confirms gradual polyhedral transformation by showing a consistent shift of the O–Si–O intratetrahedral angle from 109.5° (ambient) to 97–104° (200 GPa) with FWHM broadening from 12° to 22° and a decrease of the Si–O–Si angle from 147–155° to 115–130°.

Additionally, at 200 GPa, the coordination number analysis clearly demonstrates a shift from solely four-fold Si at ambient to mostly six-fold (octahedral), with tricluster O formation serving as a densification signal.

Young's modulus and fracture strength increase monotonically with pressure, but failure strain (embrittlement) decreases, according to the stress-strain curves. Bond compression and coordination transformation work together to cause density increases of 73–182% across the pressure range, with values approaching and surpassing the stishovite density at 200 GPa. For relaxation time is a critical kinetic parameter: longer NPT equilibration consistently produces sharper structural features, thermodynamically stable CN distributions, and superior mechanical properties.

REFERENCE

Barciela, R. M. (2024). Size effects on the fracture behavior of amorphous silica from molecular dynamics simulations. *Journal of Non-Crystalline Solids (2024), 631* , 122935.

Barciela, R. M. (2024,). Size effects on the fracture behavior of amorphous silica from molecular dynamics simulations. *Journal of Non-Crystalline Solids, 631,* , 122935.

Chowdhury S.C., Haque B.Z., Gillespie J.W. (2016) "Molecular dynamics simulations of the structure and mechanical properties of silica glass using ReaxFF." *J. Mater. Sci.* 51, 10139–10159. link.springer.com

Dewapriya, M. C. (2024). Strain rate effects on the axial tensile behavior of crystalline polyethylene: Insights from molecular dynamics simulations. *Polymer, 295,* , 126779.

Fogarty, J.C., Aktulga, H.M., Grama, A.Y., van Duin, A.C.T. & Pandit, S.A. (2010). A reactive molecular dynamics simulation of the silica–water interface. Journal of Chemical Physics, 132(17), 174704.

Grimley, D.I., Wright, A.C. & Sinclair, R.N. (1990). Neutron scattering from vitreous silica IV. Journal of Non-Crystalline Solids, 119(1), 49–64.

Häusler, M. S. (2024). Amorphous shear band formation in crystalline Si-anodes governs lithiation and capacity fading in Li-ion batteries. *Communications Materials, 5*, 163:1--13.

Huang, L. & Kieffer, J. (2004). Amorphous–amorphous transitions in silica glass. II. Irreversible transitions and densification limit. Physical Review B, 69(22), 224204.

Karki, B.B., Stixrude, L. & Wentzcovitch, R.M. (2001). High-pressure elastic properties of major materials of Earth's mantle from first principles. Reviews of Geophysics, 39(4), 507–534.

Lacks, D.J. & Rutledge, G.C. (1995). Mechanical properties of amorphous silicon dioxide. Journal of Non-Crystalline Solids, 182(1–2), 18–26.

Mozzi, R.L. & Warren, B.E. (1969). The structure of vitreous silica. Journal of Applied Crystallography, 2(4), 164–172.

Murakami, M., Kohara, S., Kitamura, N., et al. (2019). Ultrahigh-pressure form of SiO_2 glass with dense pyrite-type crystalline homology. Physical Review B, 99(4), 045153.

Park J., Kirane K. (2021) "Transitional flaw size sensitivity of amorphous silica nanostructures analyzed by ReaxFF/SiO MD." *J. Appl. Phys.* 129, 175103. pubs.aip.org

Plimpton, S. (1995). Fast parallel algorithms for short-range molecular dynamics. Journal of Computational Physics, 117(1), 1–19.

Rustad J.R., Yuen D.A., Spera F.J. "Molecular dynamics of amorphous silica at very high pressures." *Phys. Rev. B* 44, 2108. (1991) journals.aps.org

Shell, M.S., Debenedetti, P.G. & Panagiotopoulos, A.Z. (2002). Molecular structural order and anomalies in liquid silica. Physical Review E, 66(1), 011202.

Shen, G. & Lazor, P. (1995). Measurement of melting temperatures of some minerals under lower mantle pressures. Journal of Geophysical Research, 100(B9), 17699–17713.

Stixrude, L. & Karki, B. (2005). Structure and freezing of $MgSiO_3$ liquid in Earth's lower mantle. Science, 310(5746), 297–299.

Stukowski, A. (2010). Visualization and analysis of atomistic simulation data with OVITO–the Open Visualization Tool. Modelling and Simulation in Materials Science and Engineering, 18(1), 015012.

Tse, J.S. & Klug, D.D. (1992). The structure and dynamics of silicon dioxide. Physical Chemistry of Minerals, 18(5), 303–312.

van Duin, A.C.T., Dasgupta, S., Lorant, F. & Goddard, W.A. (2001). ReaxFF: A reactive force field for hydrocarbons. Journal of Physical Chemistry A, 105(41), 9396–9409.

Wallenberger, F. a. (2010). Fiberglass and glass technology: energy-friendly compositions and applications. *Springer, New York*.

Wang, Y. S.-I. (2020,). Reactive molecular dynamics simulations of wear and tribochemical reactions of diamond like carbon interfaces with nanoscale asperities under H2 gas: Implications for solid lubricant coatings,. *ACS Appl. Nano Mater.,3,*, 7297–7304.

Wang, Y. X. (2021). Non-empirical law for nanoscale atom-by-atom wear,. *Adv Sci., 8, DOI: 10.1002/advs.202002827*, 2002827.

Wang, Y. Y. (2021). Selective wear behaviors of a water-lubricating SiC surface under rotating-contact conditions revealed by large-scale reactive molecular dynamics simulations,. *J. Phys. Chem. C,125,*, 14957–14964.

Wei, B. L. (2023). Crystalline–Amorphous Nanostructures: Microstructure, Property and Modelling. *Advances in Glass and Glass-Ceramic Materials, 16(7),* , 2874.

Zha, C.S., Hemley, R.J., Mao, H.K., Duffy, T.S. & Meade, C. (1994). Acoustic velocities and refractive index of SiO_2 glass to 57.5 GPa by Brillouin scattering. Physical Review B, 50(18), 13105.

Zhang, X. L. (2024). Assessment of the mechanical and functional properties of nitinol alloys fabricated by laser powder bed fusion: Effect of strain rates. *Materials Science and Engineering: A*, 147358 , Volume 916.

Zhang, Y. C. (2021). Strain rate-dependent tensile response of glassy silicon nanowires studied by accelerated atomistic simulations. *Journal of Applied Physics, 130,* 085105.

Zohreh, F. a. (2024). Development of a ReaxFF reactive force field for ternary phosphate-based bioactive glasses. *J. Chem. Phys. 160, 184505 (2024); doi: 10.1063/5.0204589*